Detached Eddy Simulation Results for a Space Launch System Configuration at Liftoff Conditions and Comparison with Experiment

Steven E. Krist[1] and Farhad Ghaffari[2]
NASA Langley Research Center, Hampton VA 23681

Abstract

Computational simulations for a Space Launch System configuration at liftoff conditions for incidence angles from 0 to 90 degrees were conducted in order to generate integrated force and moment data and longitudinal lineloads. While the integrated force and moment coefficients can be obtained from wind tunnel testing, computational analyses are indispensable in obtaining the extensive amount of surface information required to generate proper lineloads. However, beyond an incidence angle of about 15 degrees, the effects of massive flow separation on the leeward pressure field is not well captured with state of the art Reynolds Averaged Navier-Stokes methods, necessitating the employment of a Detached Eddy Simulation method. Results from these simulations are compared to the liftoff force and moment database and surface pressure data derived from a test in the NASA Langley 14- by 22-Foot Subsonic Wind Tunnel.

Nomenclature

C_A	axial force coefficient
C_Y	side force coefficient
C_N	normal force coefficient
C_l	rolling moment coefficient
C_m	pitching moment coefficient
C_n	yawing moment coefficient
C_P	pressure coefficient
D	nominal diameter of the core stage – used as reference length
$\log(R/R_0)$	$\log_{10}$ of (|current solution residual / initial solution residual|)
M	free-stream Mach number
X, Y, Z	Cartesian coordinates
y^+	nondimensional distance from the wall in the boundary layer
α_T	total angle of attack in missile coordinate system, in degrees
ϕ_T	roll angle in missile coordinate system, in degrees
ϕ	radial angle as measured from the centerline of the vehicle, in degrees

Acronyms and Abbreviations

CAD	Computer-aided Design
CFD	Computational Fluid Dynamics
DES	Detached Eddy Simulation
ICPS	Interim Cryogenic Propulsion Stage
MPCV	Multi-Purpose Crew Vehicle
OML	Outer Mold Line

[1] Aerospace Engineer, Configuration Aerodynamics Branch, MS 499, AIAA Senior Member.
[2] Aerospace Engineer, Configuration Aerodynamics Branch, MS 499, AIAA Associate Fellow.

PBROM	Physics Based Reduced Order Method
POD	Proper Orthogonal Decomposition
RANS	Reynolds Averaged Navier-Stokes
SA	Spalart-Allmaras turbulence model
SLS	Space Launch System
SRB	Solid Rocket Booster
SST	Menter's Sheer Stress Transport turbulence model
WT	Wind Tunnel

I. Introduction

The NASA Space Launch System (SLS) is comprised of a family of advanced launch vehicles designed to provide a new capability for deep-space exploration. Analyses of the aerodynamic characteristics of the vehicles are required to provide performance estimates to the Trajectory and Guidance, Navigation, & Control groups, lineloads to the Loads and Structures groups, surface pressures to the Venting group, and boundary layer profiles to the Acoustics group. Aerodynamic databases containing this information are required for the ground wind loads, liftoff, ascent, stage separation, and descent regimes.

One of the more difficult regions of flight to assess is the liftoff regime, as flow conditions must be evaluated from total angles of attack ranging from 0^o to 90^o and roll angles from 0^o to 360^o. In addition, the assessment of launch tower effects at a total angle of attack of 90^o is required. While force and moment data, along with a limited amount of pressure data, can be efficiently obtained from a standard wind tunnel test, Computational Fluid Dynamics (CFD) simulations are indispensable in obtaining the extensive amount of surface pressure data required to generate proper lineloads and the numerous boundary layer profiles required over various vehicle sectors for acoustic analyses. However, standard state of the art Reynolds Averaged Navier-Stokes (RANS) methods are not well suited for modeling the massive flow separation on the leeward side of the vehicle as the total angle of attack is increased beyond about 15^o degrees. The deficiency of the RANS method may be ameliorated to some extent by use of the more complex and resource intensive Detached Eddy Simulation (DES) method and its variants.

A typical procedure in generating lineloads for the ascent regime involves conducting a wind tunnel test to determine the integrated force and moment coefficients, conducting CFD simulations at wind tunnel conditions to generate increments for a wind tunnel to CFD correction of the forces and moments, then employing a simple scaling procedure to correct the CFD generated lineloads such that integrated forces and moments from the lineloads match the values from the wind tunnel database. However, results from CFD simulations tend to correlate much better with wind tunnel results for the ascent problem than for the more complex liftoff problem. Consequently, application of the standard lineload correction procedure for the liftoff regime results in a database of low fidelity with large uncertainties.

In an attempt to improve the fidelity of the liftoff lineload database, a novel procedure was developed to synthesize the information from the wind tunnel test and CFD simulations through the use of a Physics-Based Reduced-Order Model (PBROM). The PBROM procedure involves the following steps: utilize a Proper Orthogonal Decomposition (POD) to transform the high-dimensional CFD surface pressure and skin-friction data into a low-dimensional modal model; project the POD modes onto the surface data to obtain the POD coefficients; assimilate the wind tunnel force and moment data to adjust the POD coefficients using the wind tunnel pressure data as constraints. The resulting PBROM can then be interrogated at any condition within the envelope covered by the database to extract corrected surface pressure and skin-friction distributions, from which the corrected lineloads can then be extracted.

Application of this novel procedure was developed for a representative SLS configuration at liftoff conditions without the launch tower. Further information on the commensurate wind tunnel test is provided in the companion paper by Pinier et al.[1], while; development of the PBROM is provided in the companion paper by Carlson et al.[2] The present paper describes the computational approach, which utilizes the DES method as encoded in the USM3D flow solver for unstructured grids. The current state of best practice procedures for implementing the DES method in USM3D, much of which was developed in unpublished work on a simplified Titan III launch configuration for

which experimental data at liftoff conditions were available, is discussed in Section II. The CFD run matrix is described in Section III, while DES simulation results are compared to experimental results in Section IV.

II. Vehicle Description and Computational Approach

The configuration analyzed in this work is a version of the 70-metric-ton crewed SLS vehicle. The outer mold line (OML) of the representative model, as defined in the Computer-aided Design (CAD) definition used to build the wind tunnel and CFD models, is shown in Figure 1. The configuration consists of the core stage with port and starboard solid rocket boosters (SRBs), each of which is attached with a set of forward and aft brackets. Mounted on top of the core stage are the Interim Cryogenic Propulsion Stage (ICPS) and the Multi-Purpose Crew Vehicle (MPCV). The CFD model incorporates all of the protuberances that were included on the wind tunnel model. The metric portion of the vehicle, upon which integrated forces and moments are tabulated, includes the core stage up until the termination of the nozzle aerodynamic fairings (does not include the black base surfaces or the cavity/sting) and the SRBs up to the cap on the SRB nozzles (purple and magenta surfaces). Note that separate lineloads are required for the core stage and the port and starboard SRBs, and these are to be computed over the entire length of the respective metric surfaces.

The NASA Tetrahedral Unstructured Software System (TetrUSS[3]), developed at NASA Langley Research Center, was used for the computational analysis of the configuration. This suite of tools includes a geometry setup graphics tool called GridTool, an unstructured grid generation program called VGRID, a grid post-processing tool named POSTGRID, and the flow solver USM3D.

Flow Solution Methodology

USM3D[4] is a cell-centered, finite volume method for solving the Euler and Navier-Stokes (N-S) equations on tetrahedral grids. In addition to the traditional RANS capability, it also provides an option for DES for use in situations involving massively separated flow. The DES method combines the more favorable aspects of RANS models with those of Large Eddy Simulation (LES) models in an attempt to capture the accuracy of the LES model with lower resource requirements than that of a full LES. Nonetheless, DES simulations require substantially larger grids than required for RANS simulations, as it is necessary to enhance the grid resolution to capture the wake system associated with the massively separated flow over the leeward side of the vehicle.

The strategies used in developing the grids and setting the input parameters for USM3D are based upon five years of work in constructing best practice procedures for analyzing the aerodynamic characteristics of the Ares family of launch vehicles, as summarized by Pao et al.[5] The spatial discretization is second-order accurate and Roe's flux-difference splitting scheme is employed to compute inviscid flux quantities across the faces of the tetrahedral cells. The midmod limiter, which is often required to maintain stable solutions for transonic and supersonic flows, is not needed for the low subsonic flow of the liftoff regime. Since significant regions of the flow are expected to be unsteady for most of the conditions within the liftoff regime flight envelope, all of the computations were run in time-accurate mode. The second-order time-accurate differencing scheme with the pseudo-time variable is employed with 10 subiterations per time step, unless the solution residual is reduced by 4 orders of magnitude prior to completion of all 10 subiterations.

USM3D provides a variety of turbulence models for closure of the N-S equations. The most commonly used turbulence models are the 1-equation Spalart-Allmaras (SA) model[6] and the 2-equation Menter's Shear-Stress Transport (SST) model[7]. The SA model tends to be the more robust of the two and the more widely used for aircraft and spacecraft aerodynamic assessments. While most of the ascent aerodynamic assessments for both the Ares and SLS programs were conducted with the SA model, the SST model was used extensively in computing jet interaction effects, where preservation of the shear layer between the freestream flow and jet plume become important. Another candidate turbulence model that is used to accurately capture free shear layers is the 2-equation k-ε model. The three turbulence models have been implemented in USM3D for both RANS and DES modes.

While the best practice procedures developed in the Ares and SLS programs are useful, they were developed for flow regimes where RANS computations were deemed to be suitable and, therefore, are not necessarily sufficient for DES computations. Hence, prior to tackling the complexity of the SLS configuration, a series of DES computations were conducted for a model of a simplified Titan III configuration for which experimental data at liftoff conditions were available. This simple configuration essentially consisted of three tubes with nose cones stacked in an arrangement similar to that of the SLS core stage and SRBs. The smaller resource requirements of the Titan III problem allowed for more timely investigations into refinements of the gridding procedures, the generation of temporal and spatial resolution studies, and assessment of the SA, SST, and k-ε turbulence models within the DES mode of operation. Results from those studies led to the selection of the k-ε turbulence model for DES computations conducted on the SLS configuration, as well as to the development of new guidelines for gridding the SLS configuration, as discussed below. In addition, the procedure for running time-accurate simulations was updated. The standard procedure had been to initiate the solutions with local time-stepping and a 1st-order spatial discretization, then once the initial transients settled out, switching to the second-order time-accurate and second-order spatial discretization. The updated procedure initiates the simulations from scratch with the second-order time-accurate and second-order spatial discretization schemes; on the Titan III configuration it was found that solutions from the updated temporal discretization procedure evolved towards a different state that more closely corresponded with the experimental results.

Grid Generation

The grid generation process begins with modification of the CAD geometry to provide a watertight OML. That geometry is imported into GridTool[8], where surface patches covering the entire OML are defined, then grouped to form components for which integrated forces and moments are to be reported. User-defined line sources and volume sources are then specified within the domain. Of primary importance in generating accurate solutions is the source specification, as the grid spacing and local density of the cells will be related to the strengths and locations of the sources, thereby allowing the user to refine the grid resolution in regions of high flow field gradients. Line sources with anisotropic stretching are typically employed at regions where components intersect or where there are sharp discontinuities in the OML surface. Volume sources in the shape of a cylinder, cone, or sphere are employed within the perimeter of the larger components of the vehicle; for cylinder and cone volume sources, the grid spacing at the two ends of the volume source can differ.

Output from GridTool is then imported to VGRID[9], which employs a three-step process to generate an unstructured volume mesh composed of tetrahedra. The first step generates a surface triangulation, the local resolution of which is controlled by the source specification. The second step employs an advancing layer method[10] to grow a boundary layer grid normal to the surface; the marching process begins by growing tetrahedral cells on the initial surface triangles, then moving out one layer at a time, with termination of the layers keyed by the local source strength. The third step employs an advancing front method[11] to mesh the inviscid flow region, gradually filling the field around the geometry and moving out to the far field boundaries. The final step in the grid generation procedure is to use the tool POSTRID to close holes in the volume grid left by the VGRID process. Options within POSTGRID allow for a variety of procedures to improve the quality of the grid, particularly in regards to reducing the number of high aspect ratio cells in the inviscid region.

A screen shot highlighting the source specification for the RANS grid is shown in Figure 2, with the view looking on to the port side of the vehicle. Solid yellow lines represent line sources, most of which utilize anisotropic stretching. Horizontally oriented line sources, as on the feed lines and systems tunnels, typically utilize a few sources, whereas vertically oriented line sources, as on the various rings and at regions of sharp planform discontinuities, are constructed from rings of line sources. The dull yellow surfaces represent volume sources, which are strung together using spheres at the nose tips, cones for regions with diameter changes, and cylinders for the constant diameter tubes. The strength of the volume sources, which specifies the grid size, varies in proportion to the diameter. Since no attempt is made to resolve the wake regions in the RANS simulations, all of the volume sources lie just within the OML surface and a single RANS grid is suitable for all roll angles. That is not the case for the DES grids, as volume sources must extend well out into the flow field in order to increase the grid density in the wake region. Hence, in order to prevent unnecessary resolution on the windward side of the domain, a separate DES grid is generated for each roll angle.

A screen shot highlighting the source specification for the DES grid for roll angles of 0^o is shown in Figure 3, where the cross-flow direction is from the bottom to the top of the figure. The line source distribution for all of the DES grids is the same as that for the RANS grid, while the volume sources generally maintain the source strength used in the RANS grid but are flush with the surface at the stagnation line and extend well out into the wake. Moreover, some of the volume sources, such as at the noses of the SRBs, are now embedded within the volume source for the SRB wake. An indication of the degree to which the wake region is refined in the DES grid is provided in Figure 4, where a cross section of the grid running through the core stage and SRBs is shown for the RANS grid and the DES grid for roll angles of 0^o; the cross-flow direction is from the bottom to the top of the figure. Note that the grid spacing from the SRB wake sources is finer than that from the core stage wake source and overrides the core stage source influence in the region of overlap. The effect of skewing the DES volume sources in order to appropriately position the refined wake for other roll angles is illustrated in Figure 5, where a cross section of the grid for roll angles of 60^o is shown.

Appropriate strategies for specifying the source strengths and distributions were developed from the lessons learned from the Titan III study. One of the more unusual findings was that the interaction of the field of sources was not as predictable as one might hope, particularly once volume sources were introduced. This precluded the use of anisotropic stretching in the specification of the volume sources, which leads to finer resolution in the boundary layer gridding than one would expect to be required. It was also found that the use of anisotropic line sources at the corners of patches was problematic, and that procedures to maintain symmetry in the surface grid to as great an extent as possible were desirable. Appropriate source strengths for the volume sources in the wakes was ascertained through a limited grid resolution study of the Titan III; the spacing in the wake grids for the various components was set such that the ratio of the nominal grid spacing to the diameter of the component was kept around 0.017; hence the source strengths for the volume sources in the wakes of the SRBs was set at 2.5, whereas the value for the volume source in the wake of the core stage was set at 5.5. This ratio lies quite close to the coarser end of the recommended spacing limits for DES studies of the circular cylinder problem. The Titan III study was also used to size the radius of the volume sources in the wakes. The spacing for the height of the first layer of cells off the wall was set at 0.01 to ensure that y^+ values over the entire surface of the vehicle remained lower than 1.0; subsequent plots of y^+ contours indicated that maximum values of around 0.7 were reached.

The RANS grid was composed of roughly 186 million cells, which makes it about 20% larger than the grids typically generated for ascent analyses for SLS configurations with substantially larger numbers of protuberances. The DES grids ranged from 438 million to 460 million cells, being dependent on the roll angle for which the grid was generated. While a grid resolution study is desirable and may yet be pursued, the existing grids represent the coarser end of a grid study.

III. CFD Run Matrix and Computer Resources

The wind tunnel test of the SLS model at liftoff conditions was conducted over a range of Mach numbers, with most of the data taken at M = 0.18 and a Reynolds number of 0.672 million based on the reference diameter. Pitch sweeps were taken at every 30^o for roll angles from 0^o to 330^o, while roll sweeps were taken for total angles of attack at 0^o, 10^o, 20^o, 25^o, 60^o, 70^o, and 90^o. Note that roll sweeps were not obtainable for incidence angles from 30^o to 55^o , as severe model dynamics were encountered over this range of conditions. Additional details on the wind tunnel test are provided in the companion paper by Pinier et al.[1]

All CFD runs were conducted at M = 0.2 rather than 0.18, but at the same Reynolds number at which the wind tunnel data were taken. Due to the expense of the DES simulations, the CFD run matrix was much smaller than what is typically specified in developing databases for the ascent regime. As a result, the minimum number of runs deemed to be necessary for proper evaluation of the PBROM procedure were selected. Roll angles were limited from 0^o to 90^o with an increment of 30^o, and roll sweeps were taken at total angles of attack of 0^o, 10^o, 30^o, 55^o, 70^o, and 90^o.

The CFD run matrix, superimposed upon a table that delineates the conditions at which wind tunnel data is available, is shown in Table 1. Note that the wind tunnel data is only available at those conditions for which the box

is colored, leaving quite a void in the matrix for total angles of attack from 35° to 50° where model dynamics issues were encountered. While the initial CFD plan was to run a roll sweep at a total angle of attack of 50°, the sparsity of wind tunnel data at those conditions necessitated the switch to 55°. Since massive flow separation does not become an issue until incidence angles exceed about15°, RANS simulations, rather than the more resource intensive DES simulations, were conducted at the lower angles of attack. Hence, the five CFD results for angles of attack at 0° and 10° are from RANS simulations, while the 16 CFD results for angles of attack from 30° to 90° are from DES simulations; this is reflected in the coloring scheme for Table 1, where the orange and red colored boxes denote conditions at which RANS or DES simulations were used, respectively.

Table 1. CFD Run Matrix and Conditions at Which Wind Tunnel Data is Available

	ϕ_T						
α_T	0	15	30	45	60	75	90
0							
1							
2							
5							
10							
15							
20							
25							
30							
35							
40							
45							
50							
55							
60							
65							
70							
75							
80							
85							
90							

WT Pressure Port Data and RANS CFD
WT Pressure Port Data and DES CFD
WT Pressure Port Data but no CFD

The CFD simulations were run using the parallel version of USM3D on the large Linux clusters of the NASA Advanced Supercomputing (NAS) facility located at NASA Ames Research Center. The RANS simulations required 140 hours using 480 processors on the Ivy Bridge nodes of the Pleiades supercomputer. The DES simulations were run using 1200 processors on the Ivy Bridge nodes and required from 200 hours to 400 hours depending on the incidence angle, with the higher incidence angles requiring greater resources. Hence, the DES simulations were anywhere from three and a half to seven times more expensive than the RANS simulations.

IV. Results

All of the RANS and the DES simulations were initiated with the second-order time-accurate and second-order spatial discretization procedures and run out in time until the time histories of the total force and moment coefficients settled into an oscillatory trend that exhibited little drift over the course of the last 20,000 iterations. At that point, the solutions were restarted to run 4000 additional time steps. Over this last run, the five solution variables were written out at each of the 158 pressure port locations at each time step, while a procedure was invoked to compute a running time average of the five solution variables within each cell throughout the entire flow domain; this time-averaged flow-field was written out at the end of the run. In order to provide the information required for the PBROM, the results were post-processed to provide time-averaged values of the various coefficients over the last 4000 time steps, including the pressure coefficient at each of the pressure ports, surface distributions of the pressure coefficient and the three components of the skin-friction coefficient, and the vehicle integrated force

and moment coefficients. The computed force and moment coefficients are compared with the liftoff force and moment database values, after which the characteristics of some specific CFD simulations are examined, including comparison of CFD and wind tunnel pressure coefficients at the wind tunnel pressure port locations.

Force and Moment Coefficient Comparisons

The CFD and wind tunnel database values of the force and moment coefficients for pitch sweeps at roll angles of 0^o, 30^o, 60^o, and 90^o are shown in Figures 6-9, respectively. Due to the sensitive nature of the data, magnitudes of the coefficients are not included. However, in order to aid in understanding the data trends, a horizontal line is provided at the zero value of the coefficient with positive values above zero, the range of the vertical scale for each coefficient is the same from one figure to the next, and the ranges of the vertical axes for the normal and side force, and for the pitching and yawing moment, are the same in each figure. The error bars in the plots are for the wind tunnel data, as extracted from the wind tunnel database. Referring back to Figure 1, note that $\phi_T = 0^o$ coincides with flow that is orthogonal to the Y-axis with the windward side of the vehicle in the positive Z direction, whereas $\phi_T = 90^o$ coincides with flow that is orthogonal to the Z-axis with the windward side of the vehicle in the negative Y direction. Although the vehicle is not symmetric about either the X-Y or X-Z planes due to various protuberances, the sizes of these protuberances are small relative to overall vehicle size. Consequently, symmetric flow features can be expected at some conditions for roll angles of 0^o and 90^o.

For the pitch sweep at $\phi_T = 0^o$, shown in Figure 6, trends and magnitudes in the normal force and pitching moment, which are by far the largest coefficients at this orientation, are well captured by the CFD. Nonetheless, the coefficient values for $\alpha_T = 55^o$ and above lie at the outer edge of the wind tunnel database error bar. Note the large magnitude of the error bars from $\alpha_T = 25^o$ to 40^o, which reflects the scarcity of data in this region (see Table 1) due to model dynamics issues. For the side force and yawing moment coefficients, the wind tunnel values remain near zero up to $\alpha_T = 20^o$, after which the values become positive, gaining significant magnitude by $\alpha_T = 30^o$, then eventually decrease back to zero by $\alpha_T = 90^o$. The CFD values for the side force and yawing moment coefficients exhibit trends that are similar to those of the wind tunnel values, but are of opposite sign and under-predict the magnitude of the wind tunnel values. The behavior of the lateral coefficient values with increasing angle of attack is characteristic of the flow progression for vehicles with a slender forebody at large incidence angles, in which symmetric vortices arise at moderate angles of attack, but further increases in angle of attack eventually lead to the collapse of the vortex on one side of the vehicle. The resultant asymmetric vortex shedding gives rise to large side force and yawing moment coefficients for a symmetric flight condition; though the flow field is unsteady, for most configurations the asymmetric vortex pattern is stable, as is the vortex pattern with the opposite orientation. Hence, it is not surprising that the CFD appears to have picked up asymmetric vortex shedding with the opposite orientation from that exhibited in the wind tunnel test.

The other set of conditions at which strong asymmetric vortex patterns can be identified is for roll angles of 90^o. Force and moment coefficient plots for the pitch sweep at $\phi_T = 90^o$, shown in Figure 9, exhibit similar behavior to that seen for the pitch sweep at $\phi_T = 0^o$, but in this case the side force and yawing moment coefficients are well captured with the CFD while evidence of asymmetric vortex shedding is apparent in the behavior of the normal force and pitching moment coefficients. However, the wind tunnel database in this case suggests that the asymmetric vortices switch orientation, then switch back again, between $\alpha_T = 35^o$ and 45^o and between $\alpha_T = 65^o$ and 75^o. Similar to the trends at $\phi_T = 0^o$, the CFD under-predicts the magnitude of the effect that the asymmetric vortices have on the normal force and pitching moment coefficients and captures the orientation opposite from that exhibited in the wind tunnel test, except at $\alpha_T = 70^o$.

Force and moment coefficients for the pitch sweep at $\phi_T = 30^o$, shown in Figure 7, indicate that the CFD correlates with the wind tunnel database about as well as it does for the $\phi_T = 0^o$ pitch sweep. However, the CFD values of the side force at $\alpha_T = 70^o$ and 90^o, and the values of the rolling moment at $\alpha_T = 55^o$ and 90^o, lie outside the range of the wind tunnel database error bars. The correlation between wind tunnel database and CFD force and moment coefficient trends is reasonable for the pitch sweep at $\phi_T = 60^o$, shown in Figure 8, with the exception of the odd trends in the wind tunnel database coefficients over the angle of attack range from 30^o to 55^o; this is also the area of the flow field regime where the wind tunnel data is the sparsest (see Table 1).

Perhaps the largest unresolved issue that arises from the computational and experimental analyses is whether or not the asymmetric wake is bi-stable in nature or whether there is a single preferred orientation for the asymmetric vortices. The fact that the CFD simulations predicted the opposite orientation from the wind tunnel test at roll angles of 0^o suggests that the nature of the system is bi-stable. The behavior of the wind tunnel database at roll angles of 90^o, where the orientation switches from one mode to the next then back again at two different locations along the pitch sweep, coupled with the repeatability of the wind tunnel runs at roll angles of 0^o, suggests that there may be a preferred orientation, possibly set by the location of the protuberances. Of course, the flow may just as well have a bi-stable mode over various ranges of conditions while having a preferred orientation elsewhere.

DES Solutions at $\alpha_T = 70^o$, $\phi_T = 0^o$

In the course of developing the current set of best practice procedures for the SLS liftoff problem, a number of simulations were conducted at the $\alpha_T = 70^o$, $\phi_T = 0^o$ condition in order to assess the effects of varying a number of input parameters. Unfortunately, this turned out to be one of the conditions where the solution took the longest to settle out, so the results are not quite as representative of the behavior of the lower incidence angle simulations as initially expected.

Time histories of the residual and force and moment coefficients for the DES simulation with the k-ε turbulence model, using the current set of best practice procedures, are shown in Figure 10. The behavior of the solution and turbulence residuals over the time steps is shown on the top left, the behavior of the subiterations for the last 20 time steps is shown on the top right, and the histories of the force and moment coefficients are shown on the lower left and right, respectively. The solution residual behaves nicely, with the residual reduction reaching 4 orders of magnitude within the first 40,000 iterations; by the end of the run, the subiteration history for the solution residual reaches the four order magnitude reduction criteria within nine subiterations, rather than using the ten subiterations that is the maximum allowed. The turbulence residual, however, remains flat. This is due to setting the freestream turbulence intensity level to a relatively large value of 0.001, which ensures that the flow transitions from laminar to turbulent as early as possible. When a lower intensity level is used, the subiteration convergence behavior becomes more like one would expect, but the level of convergence over the course of the simulation shows a lot of variation. The force and moment histories are plotted on different vertical axes, but the same range is used for the normal and side force, and for the pitching and yawing moment. The side force and yawing moment settle down relatively quickly, oscillating with little drift by around 150,000 iterations; note that the coefficients are oscillating about the zero value, indicating that the CFD is not picking up the asymmetric vortex shedding that is captured in the wind tunnel test. The normal force and pitching moment do not settle down until about 350,000 iterations. This is one of the cases that took the longest for the force and moment histories to settle out. The general trend was that the higher the angle of attack, the longer it took for the DES runs to settle down, with the $\phi_T = 30^o$ cases settling down within 200,000 iterations and the $\phi_T = 90^o$ cases settling down within 400,000 iterations.

The propagation of the wake on the leeward side of the vehicle is displayed in Figure 11, where Mach contours (blue is near zero, red is greater than freestream) for the instantaneous flow at the last time step are shown at eight selected crossflow stations, highlighting the fine eddy content of the solution. The broad spanwise extent of the wakes affirm the need to extend the DES grid refinements in the spanwise direction well out past the spanwise extent of the SRBs. The planform plot at the center of the figure shows surface pressure coefficient contours (blue is negative, red is positive) for the instantaneous flow on the leeward side of the vehicle. The planform plot is overlaid with black vertical lines indicating the eight crossflow stations at which the Mach contours were extracted. The thicker black lines indicate the six stations at which rings of pressure ports were located on the wind tunnel model, namely, at station (Sta) 1550 on the MPCV, Sta 2160 on the cone of the ICPS, Sta 2830 that cuts through the nose cones of the SRBs, Sta 3200 and Sta 4300 that cut through the core stage and SRBs, and Sta 4776 that cuts through the aft skirts of the SRBs and the wind tunnel sting. Additional pressure ports were located along a line of constant radial angle $\phi = 30^o$, as measured from the centerline of the vehicle, and runs down the leeward side of the MPCV, ICPS, and core stage.

Figure 12 shows the wind tunnel model pressure port locations superimposed over the CFD cross sectional geometry at two longitudinal stations along the vehicle, namely, at stations 3200 and 4300. In the compressed vertical scale of the plot, the port SRB (left), core stage (center), and starboard SRB (right) cross sections are rendered as ovals rather

than circles. Note that the station cuts pick up the feedlines at Y=0 and the slightly offset systems tunnel near Y=0 on the core stage, along with the SRB systems tunnels at Z=0.

Plots of the wind tunnel data and CFD surface pressure coefficient data from the DES simulation with the k-ε turbulence model at $\alpha_T = 70^o$, $\phi_T = 0^o$ are shown in Figures 13-15. In each of the plots, the wind tunnel data are shown with the black open circles. The time-averaged CFD values at the ports are shown with red filled circles and the error bars, rather than showing the standard deviation, indicate the minimum and maximum levels attained by the pressure coefficient over the last 4000 time steps. The thin blue line shows the instantaneous pressure distribution at the last time step, whereas the green line shows the time-averaged pressure distribution over the last 4000 time steps; as such, the green line should run through the center of the red circles and the blue line should lie within the max/min error bars. Note that the plots use the aerodynamic convention for plotting the pressure coefficient; i.e., the vertical axis direction is reversed from the usual orientation.

The most striking feature in the pressure coefficient plots at stations 1550, 2160, and 2830, shown in Figure 13, is the large difference in magnitude between the maximum and minimum values at ports on the leeward side of the vehicle. As expected, the correlation between wind tunnel and CFD coefficient values is the best on the windward side of the vehicle, while some fairly large discrepancies arise on the leeward side. At stations 1550 and 2160, the largest discrepancies between wind tunnel and CFD values occur at the sides of the vehicle, with the CFD over-predicting the amount of suction. At station 2830, which cuts through the core stage and the nose cones of the SRBs, the pressures on the core stage are in fairly good agreement everywhere, whereas pressures on the port SRB (left) are in much better agreement than the pressures on the starboard SRB. However, the computed pressures on the two SRBs are nearly mirror images of each other; it is the wind tunnel pressures that show much more suction on the port SRB leeward surface than on the starboard SRB, providing an indication that the wind tunnel results are affected by an asymmetry in the flow that is not present in the CFD results.

At stations 3200 and 4300, shown in Figure 14, there is little asymmetry in either the wind tunnel or CFD trends. The wind tunnel and CFD results are in quite good agreement, with the largest discrepancies occurring near the gaps between the SRBs and the core stage. Oddly enough, the CFD over-predicts the amount of suction in the gaps at station 3200, but under-predicts the amount of suction in the gaps at station 4300. The agreement between wind tunnel and CFD results is quite good on the aft skirt at station 4776, shown in Figure 15, despite all of the protuberances packed into that area. In fact, the aft skirt is the one area where wind tunnel and CFD results are in good agreement for all of the flow conditions that were computed. Pressure coefficients along the line of pressure ports located on the leeward side of the core stage at an orientation of $\phi = 30^o$ are shown in the lower portion of Figure 15 (note that the vertical black lines indicate the six stations where the rings of pressure ports are located). The wind tunnel and CFD results are in fairly good agreement everywhere except at the most upstream port on the MPCV, where the wind tunnel and CFD trends head in opposite directions; while it is tempting to dismiss the discrepancy as being due to a bad pressure port, the same discrepancy (not shown) shows up in the $\alpha_T = 55^o$, $\phi_T = 0^o$ plot, but not in the other 0^o roll angle plots at $\alpha_T = 10^o$, 30^o, or 90^o.

Since the k-ε model was selected for use based on results from the Titan III studies, upon completion of all of the runs needed to construct the lineloads database, use of the SA and SST turbulence models was re-examined on the present SLS configuration by running DES simulations at the $\alpha_T = 70^o$, $\phi_T = 0^o$ condition. The integrated force and moment results from simulations using the three turbulence models turned out to be quite similar, with the largest difference being around 8%. Plots of the wind tunnel and CFD pressure coefficient data for the three DES simulations at selected stations are shown in Figures 16 and 17, with the time-averaged results for the SA model in red, SST model in blue, and k-ε model in green. Plots for the first three rings of pressure ports, shown in Figure 16, suggest that the SST model provides a slightly better correlation with the wind tunnel results on the MPCV at station 1550 and the ICPS at station 2160. However, on the cut through the nose cones of the SRBs at station 2830, the degree to which the CFD and wind tunnel data are correlated varies. There is significant asymmetry in the wind tunnel data while symmetry is fairly well preserved in the CFD data from all three models. In general, the k-ε model is in better agreement with the wind tunnel data on the port SRB, the SST model is in better agreement on the starboard SRB, while the SA model over-predicts the expansion on both sides of both SRBs. Further back on the vehicle at station 4300, as shown in Figure 17, there is little to distinguish between the three models, though the SA model does a slightly better job of capturing the expansion of the flow in the gaps between the SRBs and the core stage. Pressures along the line of ports located on the leeward side of the core stage at an orientation of $\phi = 30^o$,

shown in the lower portion of Figure 17, indicate that results from the three models are in fairly good agreement except in the region of the ICPS; forward of station 2160 where the MPCV transitions to the ICPS, the k-ε result predicts less suction than the SA or SST results, while aft of station 2160 where the ICPS transitions to the core stage, the k-ε result predicts a larger expansion of the flow than the SA or SST results. While it is tempting to blame the anomalous behavior of the k-ε result on a well documented weakness of the model in flows with regions of large pressure gradients[12], similar issues in the region of the ICPS do not arise at other flow conditions.

The similarity between the results for the three turbulence models was unexpected, as significantly different results from the three models were obtained in the Titan III simulations. The most likely reason for the improved correlation of the three models on the SLS configuration is due to the influence of the protuberances on the SLS. In particular, at the 0^o roll angle that was assessed, the systems tunnels on the outboard sides of the SLS SRBs (as indicated in the cross-sections shown in Figure 12) are likely to fix the location of the separation at the same position for all three turbulence models, whereas the Titan III model had no protuberances. Consequently, it is expected that correlation between the three models on the SLS configuration would decrease at roll angles other than 0^o or 90^o. Another possible reason for the improved correlation between the three models is the refinements that were made to the gridding procedures for the SLS application. Overall, there appears to be a slight preference for the SST model for use in this application, though significant additional work would be required to confirm such an assessment.

Issues with Opposite Orientations of the Asymmetric Vortices

As discussed in the introduction, the surface pressure and skin-friction distributions from the CFD simulations are to be used to develop the POD modes within a PBROM, after which the wind tunnel force and moment data are used to adjust the POD coefficients while applying the wind tunnel surface pressure data as constraints. The PBROM is then used to produce corrected surface pressure and skin-friction distributions at selected conditions, from which corrected lineloads for the core stage and SRBs are developed. Hence, the magnitude and distribution of the corrections to the lineloads will be related to the differences between the wind tunnel and CFD force and moment and surface pressure data. As indicated in the force and moment coefficient plots for pitch sweeps at $\phi_T = 0^o$ and 90^o, shown in Figures 6 and 9, respectively, most of the CFD simulations capture an asymmetric vortex pattern with the opposite orientation of that exhibited in the wind tunnel test (the exception being at $\alpha_T = 70^o$, $\phi_T = 90^o$). Consequently, the wind tunnel and CFD data sets provide quite a challenge for the PBROM, as it must take the CFD data that is influenced by asymmetric vortices at one orientation and correct that data to reflect the characteristics of the wind tunnel data that is influenced by asymmetric vortices of the opposite orientation.

The most prominent case is at $\alpha_T = 30^o$, $\phi_T = 0^o$, for which development of the asymmetric vortex pattern in the DES k-ε simulation is shown in Figure 18; contours on the planform view are of the time-averaged pressure coefficient on the leeward side of the vehicle (blue is negative, red is positive) and cross-section plots are of the time-averaged Mach contours (blue is near zero, red is greater than freestream). It is evident from the cross section plots that the vortex collapses on the starboard side of the vehicle (right side of the cross-section plots), resulting in significantly more negative pressure coefficient contours on the port side of the vehicle (bottom of the planform plot), thereby leading to the generation of a significant negative side force coefficient.

The magnitude of the correction to the pressure field that must be generated in the PBROM procedure can be gleaned from Figure 19, where plots of the wind tunnel and CFD pressure coefficient data for the DES simulation with the k-ε turbulence model at $\alpha_T = 30^o$, $\phi_T = 0^o$ are shown at stations 3200 and 4300. The red line shows the actual CFD values, whereas the blue line shows the CFD values but plotted against the negative values of the Y coordinate, thereby giving an estimate of what the CFD pressures would have been if the CFD had captured the orientation of the asymmetric vortices exhibited in the wind tunnel test. It is evident that the actual CFD results substantially over-predict the amount of suction on the port SRB and port side of the core stage, while under-predicting the amount of suction on the starboard SRB and starboard side of the core stage. However, upon reversing the Y coordinate of the CFD data, very good agreement with the wind tunnel pressure values is obtained. Hence, the correction to the CFD derived pressure field that is to be made in the PBROM in order to capture the vortex pattern exhibited in the wind tunnel test, as expressed in the wind tunnel force and moment and pressure data,

will be substantial. Conversely, if the DES simulation had captured the same asymmetric vortex orientation exhibited in the wind tunnel, the correction to the CFD derived pressure field would be quite small.

Upon completion of the simulations required to fill out the CFD run matrix and sending off the data package for processing with the PBROM procedure, a RANS solution was generated with the k-ε turbulence model on the RANS grid at the $\alpha_T = 30^o$, $\phi_T = 0^o$ flow condition. Unlike the DES solution, the RANS solution captured the asymmetric vortex pattern with the same orientation as that exhibited in the wind tunnel test. Plots of the surface pressure coefficient from the wind tunnel data and CFD results for the RANS and DES simulations with the k-ε turbulence model are shown in Figures 20-22; note that the DES results are once again plotted against the negative values of the Y coordinate in order to provide an indication of what could be expected from a DES simulation if it had captured the same orientation of the asymmetric vortex. While there are a few data points across the seven plots at which the RANS results are in better agreement with the wind tunnel data then the DES results, there is a clear preference for the DES results, as overall it does a much better job in capturing the trends of the wind tunnel data. Nonetheless, the RANS results are quite respectable, which came as a surprise since RANS results obtained in the Titan III simulations were notably inferior to DES results.

The essential problem to resolve is how to accommodate the asymmetric vortex issue, particularly within the framework of a PBROM, for the case in which the CFD and wind tunnel results exhibit opposite orientations. In this case, where the RANS results captured the same orientation as exhibited in the wind tunnel test while the DES results captured the opposite orientation, the PBROM results are likely to be improved by incorporating RANS results at the $\alpha_T = 30^o$, $\phi_T = 0^o$ flow condition, and perhaps at the $\alpha_T = 55^o$, $\phi_T = 0^o$ flow condition as well, provided that the RANS solutions consistently pick up the same orientation at higher angles of attack. Hence, the question arises as to whether there is a way to promote the development of a specific orientation within the CFD simulations. The only attempt made to date was to run the RANS k-ε simulation on the DES grid for the $\alpha_T = 30^o$, $\phi_T = 0^o$ flow condition, for which the asymmetric vortices were in fact established with the same orientation exhibited in the wind tunnel; however, upon restarting the run using the DES mode, the asymmetric vortices flipped back to the opposite orientation. Hence, the opposite orientation of the asymmetric vortices that is captured in the RANS and DES solutions arises due to differences in the solution methodology rather than to differences in the grids.

V. Conclusions

Results from a combination of DES and RANS simulations on a representative SLS configuration at liftoff conditions were compared against force and moment coefficients and surface pressure data at 158 port locations from a test conducted in the NASA Langley 14- by 22-Foot Subsonic Wind Tunnel. While the CFD and wind tunnel results were found to be in moderately good agreement, significant improvements to the CFD procedures are required to improve the correlation between the two data sets, particularly if the CFD is to be the sole source from which lineload databases are to be generated. Fortunately, in this case the CFD data was to be employed within a PBROM that synthesized the wind tunnel and CFD data to provide a corrected lineload database and, as shown in the companion paper by Carlson et al.[2], within the framework of that procedure, the CFD results appear to be sufficient.

It is apparent from this study that there are numerous areas ripe for further investigation as to the most appropriate manner in which to run USM3D in DES mode for the liftoff problem. Perhaps the highest priority is to investigate the newly installed Delayed Detached Eddy Simulation (DDES) capability in USM3D, as DDES has been shown to be superior to DES in numerous applications. While limited grid and temporal resolution studies with USM3D have been conducted on the Titan III liftoff problem, similar studies have yet to be conducted for the SLS liftoff problem, but are unlikely to be pursued until the DDES mode has been evaluated. Another issue to be resolved is identification of the most appropriate turbulence model to use within the DES mode, as no clear preference was identified for the SA, SST, or k-ε turbulence model. Moreover, there appears to be some need to investigate some of the parameter settings for the turbulence models, particularly in regard to the freestream turbulent intensity level. Recent unpublished work also suggests that more appropriate procedures for performing the temporal integration are available, particularly in regard to using a much larger initial time step to more quickly settle the flow, along with using the Newton subiteration scheme rather than the pseudo time variable scheme employed in this work. An additional issue arises for the situation realized in this work, where the CFD captured asymmetric vortex shedding

with the opposite orientation from that exhibited in the wind tunnel test; the question as to whether there is a way to promote the development of a specific orientation within the CFD simulations has yet to be resolved. While the number of topics to be explored indicates that implementation of the DES mode within USM3D has yet to reach a mature state, all of the above issues are being pursued, though on simpler canonical problems, such as the circular cylinder in cross-flow and the tangent ogive forebody at large angles of incidence.

Acknowledgments

Dr. Mohagna Pandya of NASA Langley Research Center provided the version of USM3D utilized in this study. Much of the work on the Titan III configuration that was used in developing an initial set of best practice procedures for implementing the DES method was conducted by Jake Tynis of Old Dominion University.

References

[1] Pinier, J. T., Erickson, G. E., Paulson, J. W., Tomek, W. G., Bennett, D. W. and Blevins, J. A., "Space Launch System Liftoff and Transition Aerodynamic Characterization in the NASA Langley 14- by 22-Foot Wind Tunnel", AIAA Science and Technology Forum and Exposition (SciTech 2015), Kissimmee, Florida, January 5-9, 2015.
[2] Carlson, H. A., Verberg, R., Pinier, J. T., and Krist, S. E. , "Reduced-order Model for NASA Space Launch System Liftoff Aerodynamics", AIAA Science and Technology Forum and Exposition (SciTech 2015), Kissimmee, Florida, January 5-9, 2015.
[3] Frink, N. T.; Pirzadeh, S.Z.; Parikh, P.C.; Pandya, M.J.; and Bhat, M.K., "The NASA Tetrahedral Unstructured Software System", The Aeronautical Journal, Vol. 104, No. 1040, October 2000, pp. 491-499.
[4] Frink, N. T., "Three-Dimensional Upwind Scheme for Solving the Euler Equations on Unstructured Tetrahedral Grids", Ph. D. Dissertation, Virginia Polytechnic Institute and State University, September 1991.
[5] Pao, S.; Vatsa , V.; Abdol-Hamid, K. S.; Pirzadeh, S. J. A.; Klopfer, G; Taft, J.R.; and Parlette, E. B., "Best Practice for Ascent Aero Analysis for the Ares I Configurations", 55th JANNAF Interagency Propulsion Meeting, May 12-16, 2008.
[6] Spalart, P.; and Allmaras, S.A., "One-Equation Turbulence Model for Aerodynamic Flows." AIAA 92-0439, January 1992.
[7] Menter, F.R., "Improved Two-Equation k-omega Turbulence Models for Aerodynamic Flows." NASA TM-103975, October 1992.
[8] Samareh, Jamshid, "GridTool: A Surface Modeling and Grid Generation Tool," Proceedings of the Workshop on Surface Modeling, Grid Generation and Related Issues in CFD Solutions, NASA CP-3291, May 9-11, 1995.
[9] Pirzadeh, S., "Advanced Unstructured Grid Generation for Complex Aerodynamics Applications." AIAA-2008-7178, August 2008.
[10] Pirzadeh, S., "Three-Dimensional Unstructured Viscous Grids by the Advancing Layers Method." AIAA Journal, Vol. 34, No. 1, January 1996, pp. 43-49.
[11] Lohner, R., and Parikh, P., "Three-Dimensional Grid Generation by the Advancing Front Method." International Journal for Numerical Methods in Fluids Volume 8, pp. 1135-1149 (1988).
[12] Wilcox, D. C., "Turbulence Modeling for CFD", Second Edition, Anaheim DCW Industries, 1998, pp. 174.

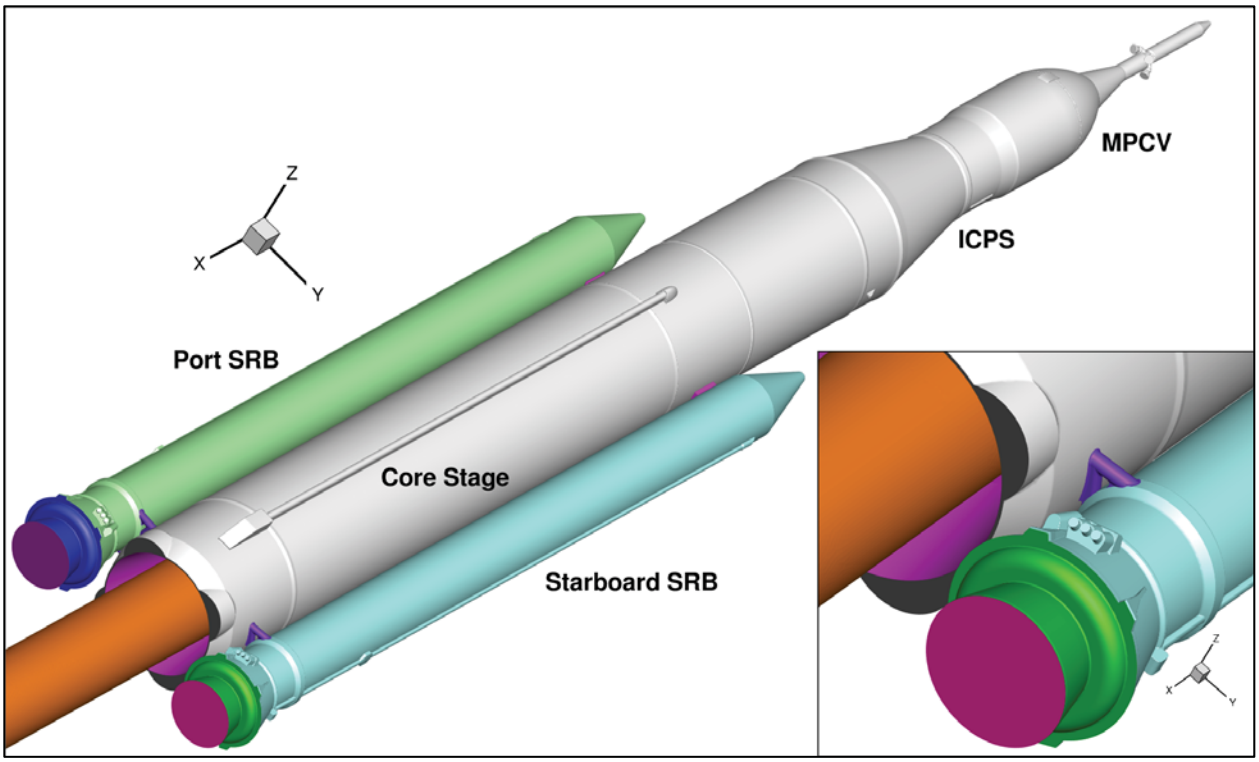

Figure 1. OML of the wind tunnel and CFD models for the representative SLS configuration.

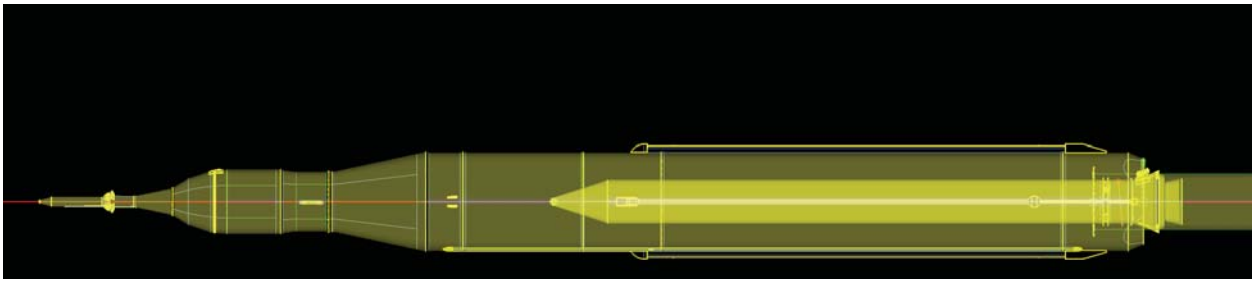

Figure 2. Port side view of the line and volume source distribution for the RANS grid.

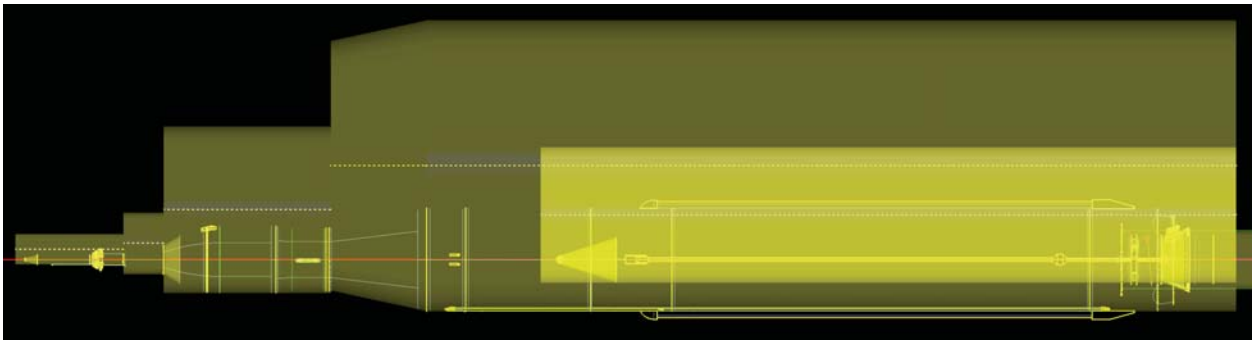

Figure 3. Port side view of the line and volume source distribution for the DES grid for flow conditions with a roll angle of 0^{o}; the cross-flow direction would be from the bottom to the top of the figure.

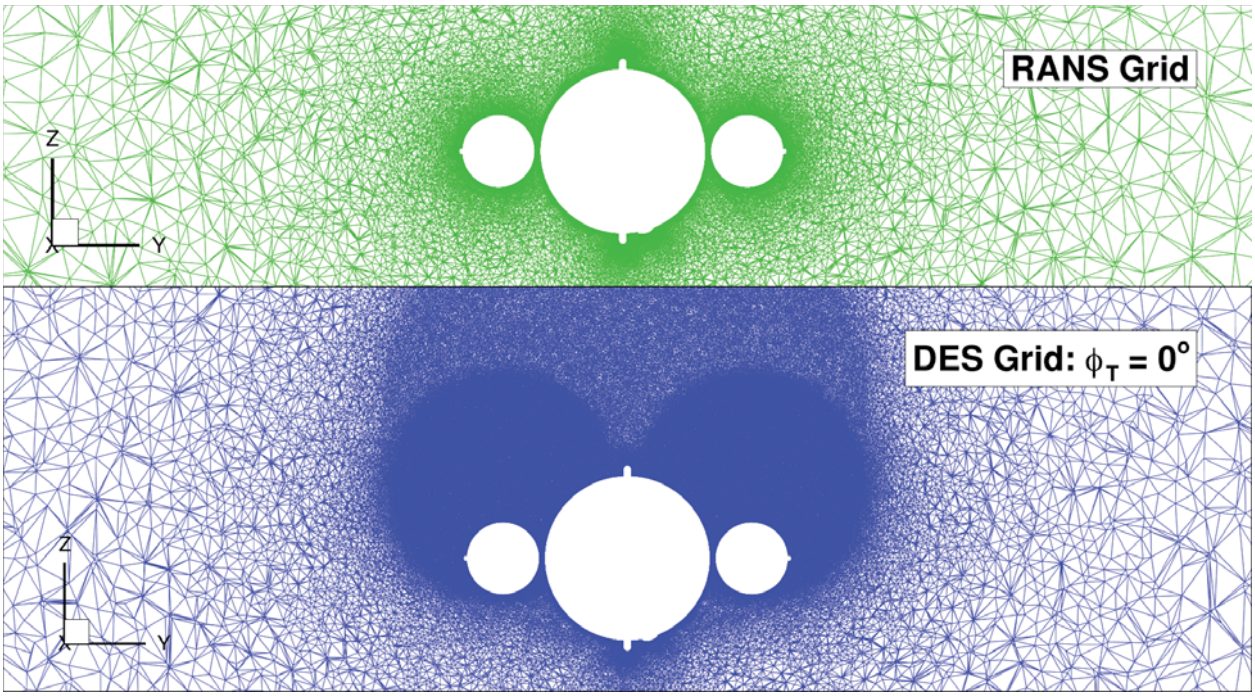

Figure 4. Crosscuts of the RANS and DES grids for flow conditions with a roll angle of 0^o; the cross-flow direction would be from the bottom to the top of the figure.

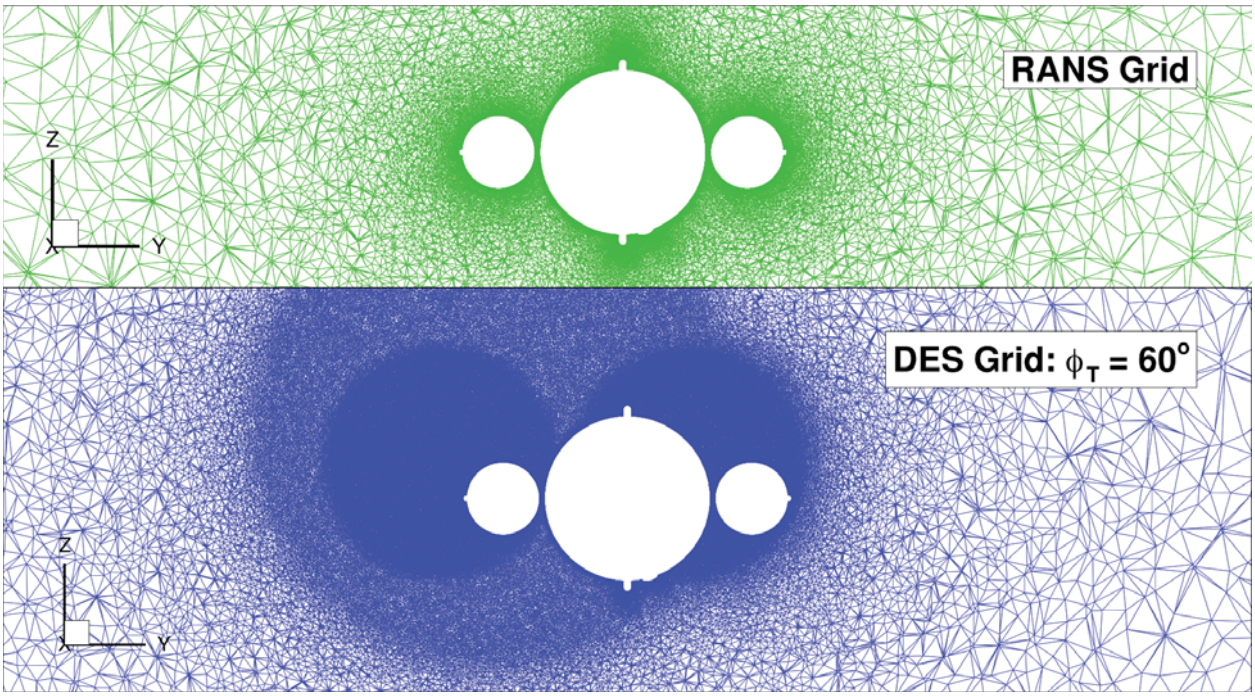

Figure 5. Crosscuts of the RANS and DES grids for flow conditions with a roll angle of 60^o; the cross-flow direction would be from the bottom right corner to the top left corner of the figure.

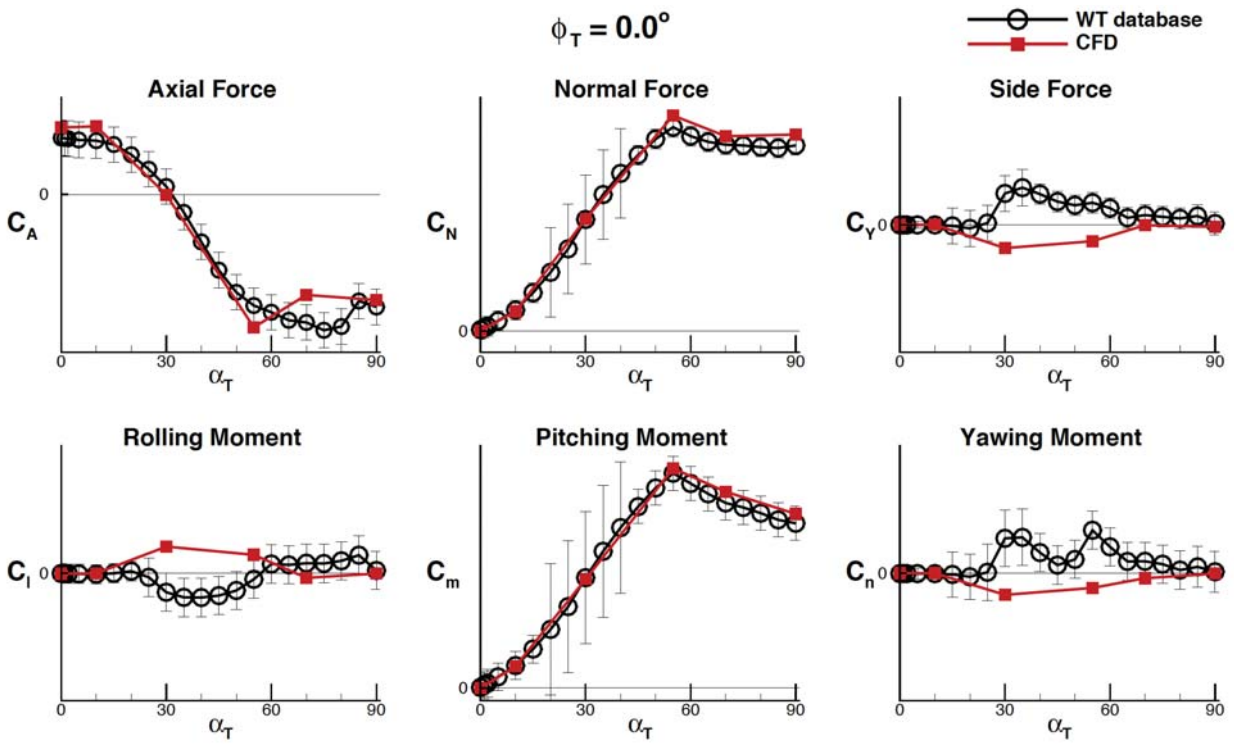

Figure 6. Wind tunnel database (black with grey error bars) and CFD derived force and moment coefficients for a pitch sweep at $\phi_T = 0^o$.

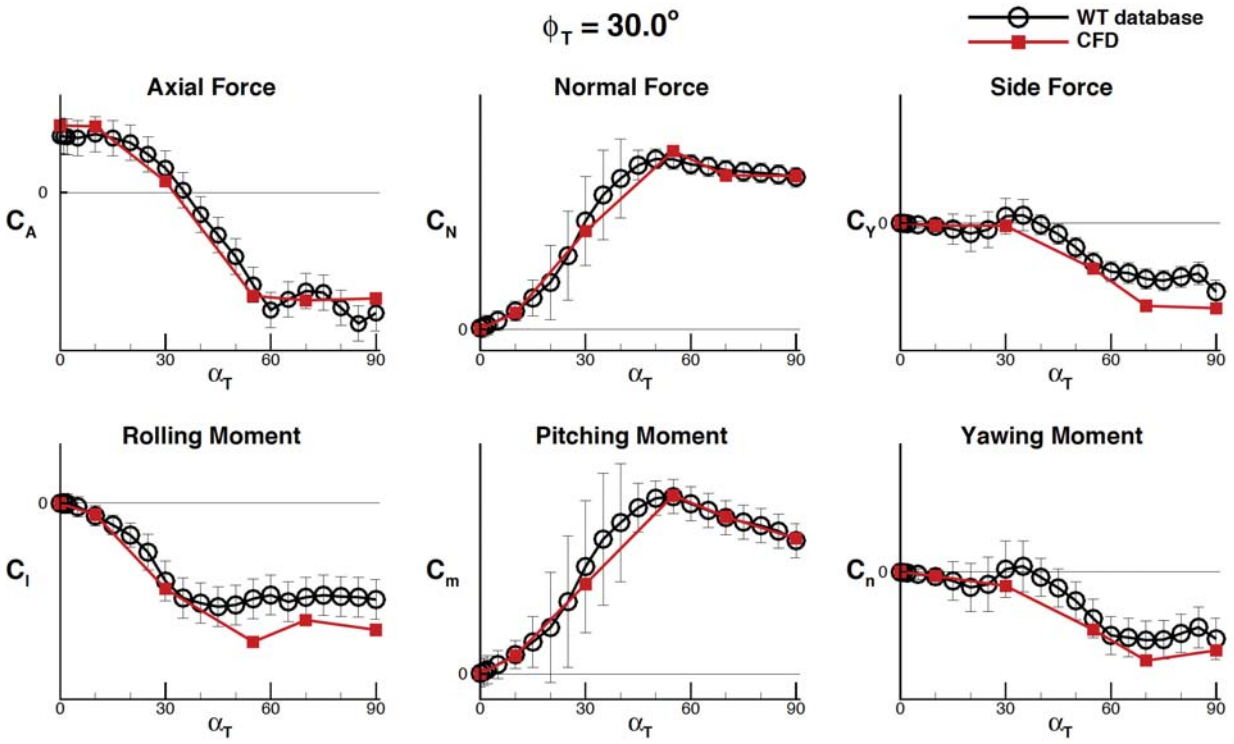

Figure 7. Wind tunnel database (black with grey error bars) and CFD derived force and moment coefficients for a pitch sweep at $\phi_T = 30^o$.

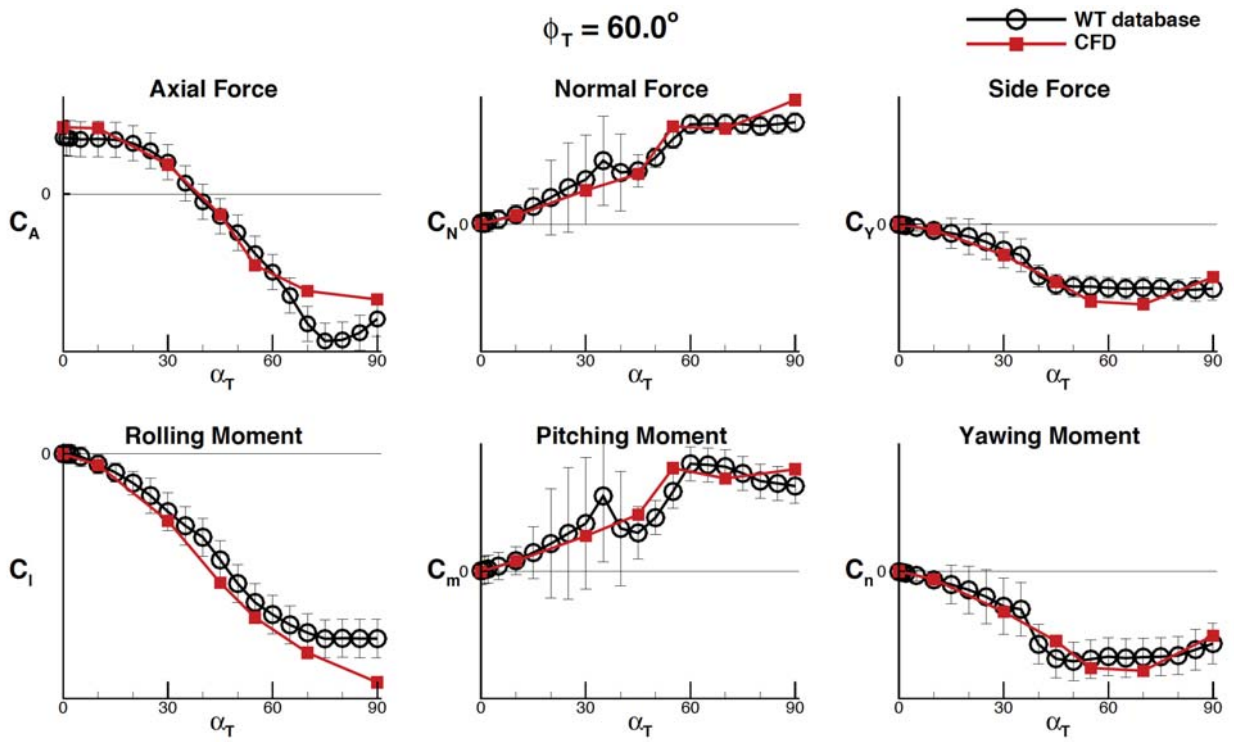

Figure 8. Wind tunnel database (black with grey error bars) and CFD derived force and moment coefficients for a pitch sweep at $\phi_T = 60^o$.

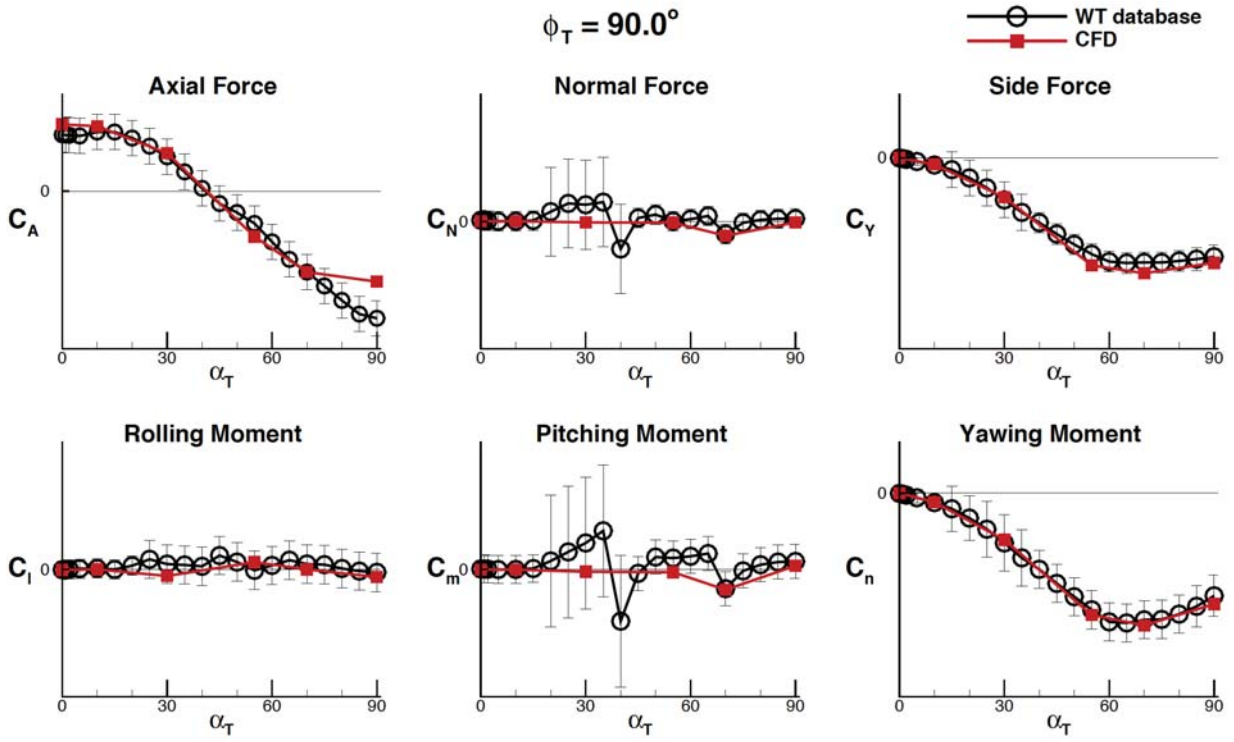

Figure 9. Wind tunnel database (black with grey error bars) and CFD derived force and moment coefficients for a pitch sweep at $\phi_T = 90^o$.

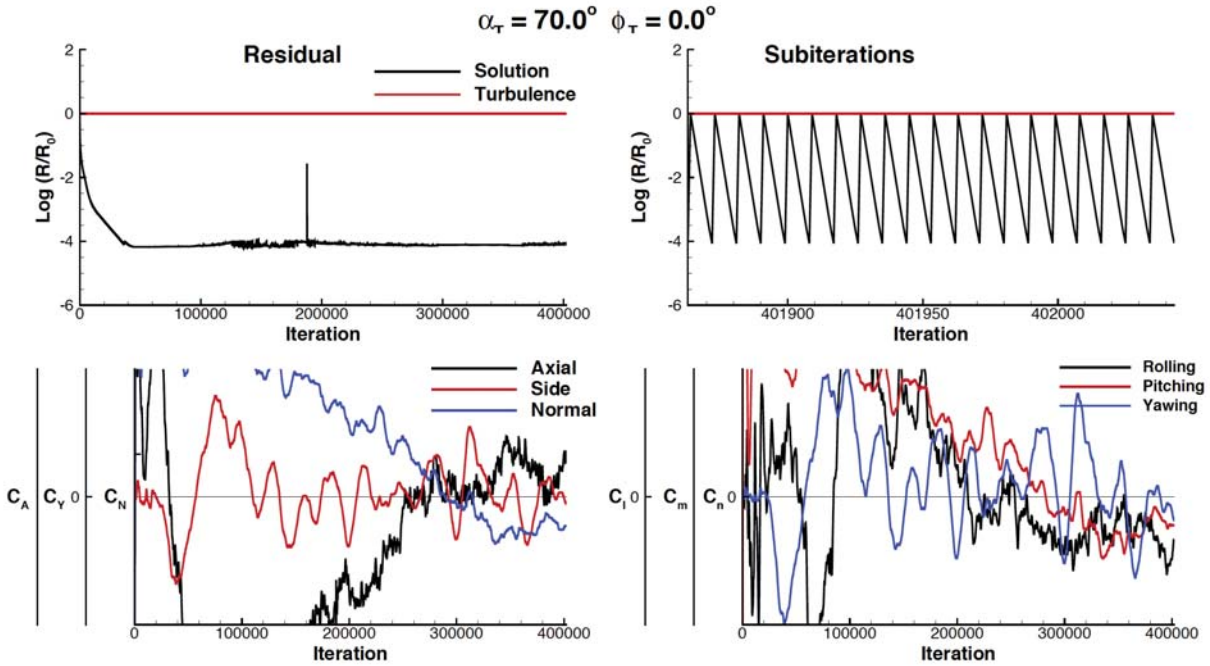

Figure 10. Time history of the residuals and the force and moment coefficients for the DES k-ε simulation at $\alpha_T = 70^o$, $\phi_T = 0^o$.

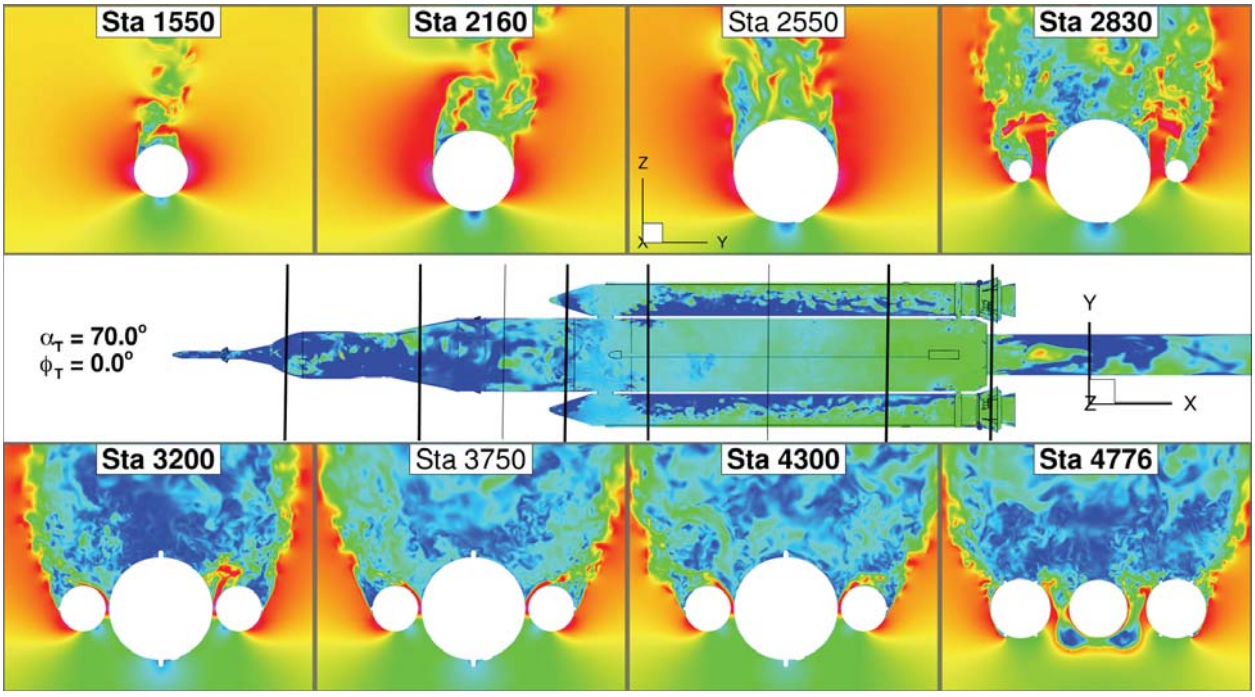

Figure 11. Instantaneous leeward surface pressure coefficient (planform) and crossflow Mach contours from the DES k-ε run at $\alpha_T = 70^o$, $\phi_T = 0^o$.

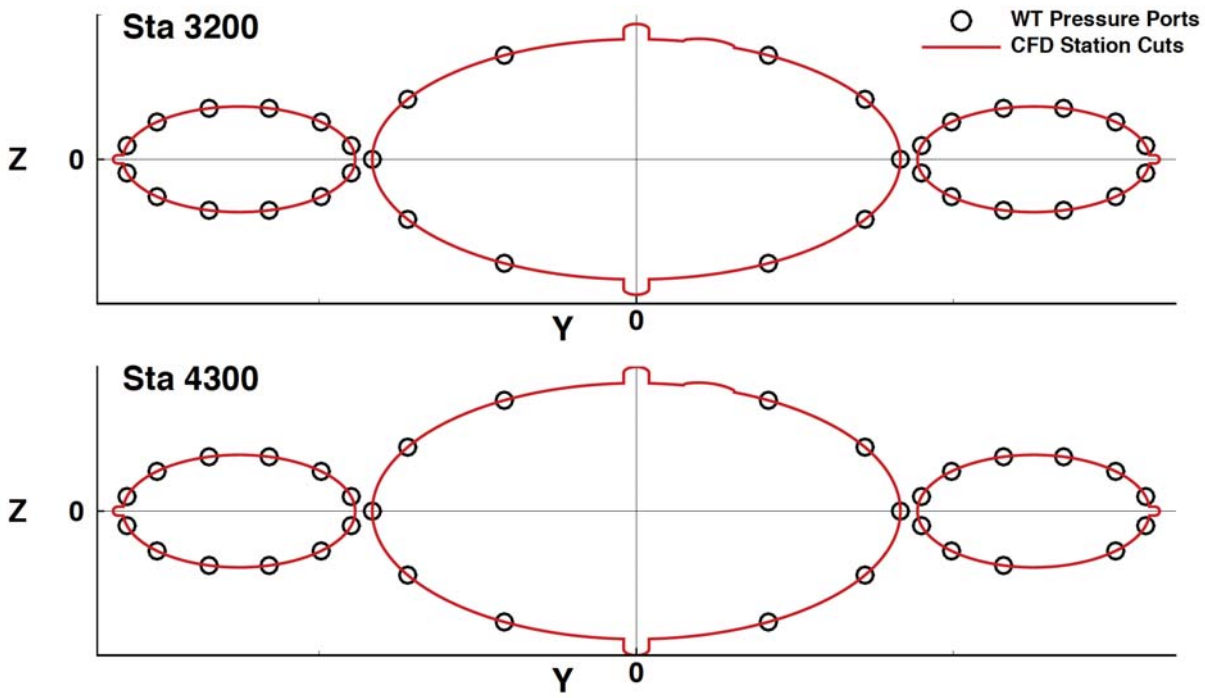

Figure 12. Wind tunnel model pressure port locations superimposed over the CFD model cross section. From left to right the cross sections are of the port SRB, the core stage, and the starboard SRB.

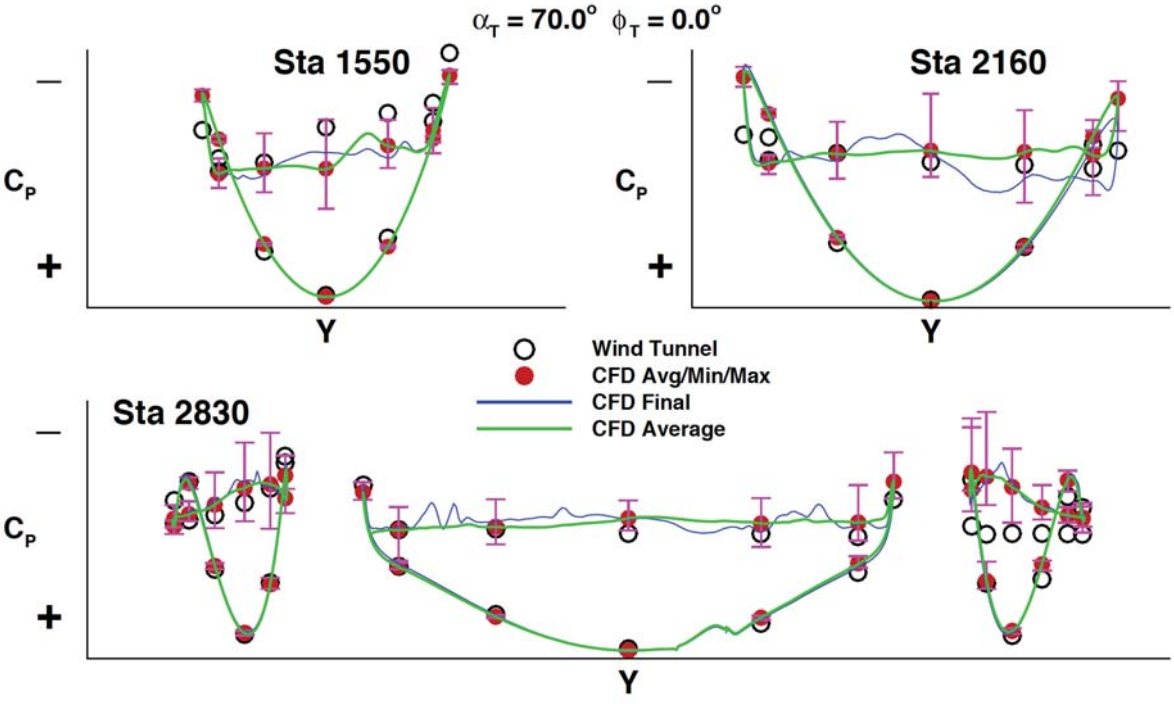

Figure 13. Pressure coefficient from wind tunnel data and CFD DES k-ε results for $\alpha_T = 70^o$, $\phi_T = 0^o$ at stations 1550, 2160, and 2830.

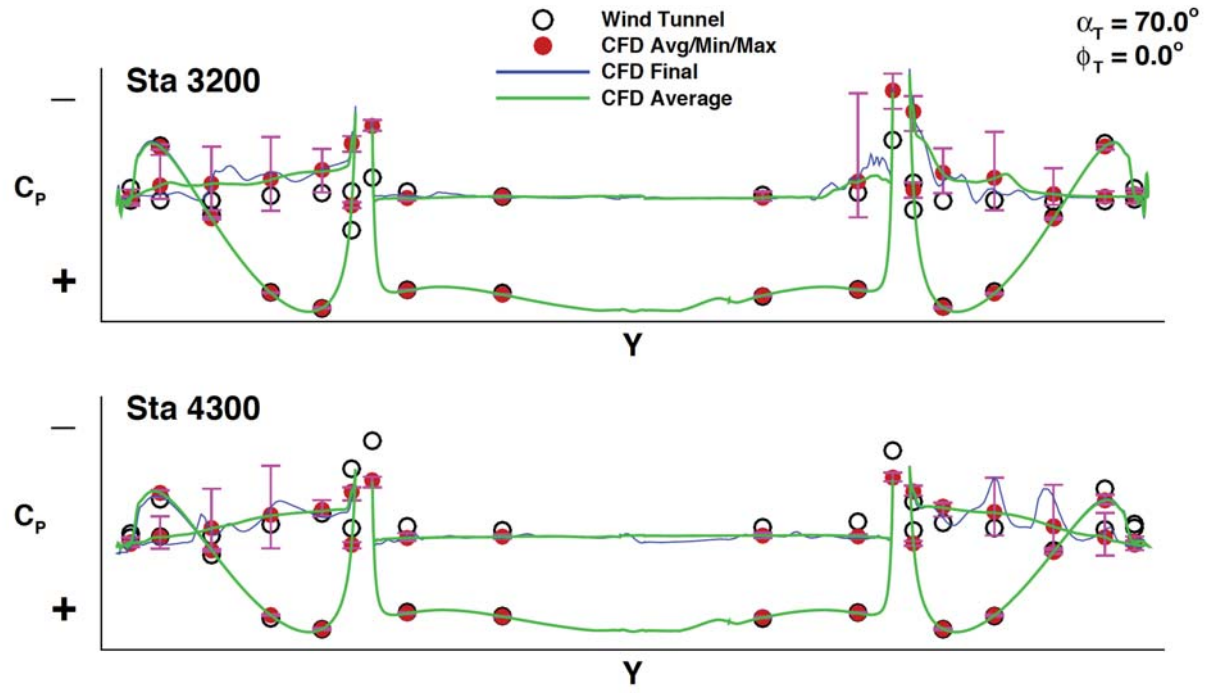

Figure 14. Pressure coefficient from wind tunnel data and CFD DES k-ε results for $\alpha_T = 70^o$, $\phi_T = 0^o$ at stations 3200 & 4300.

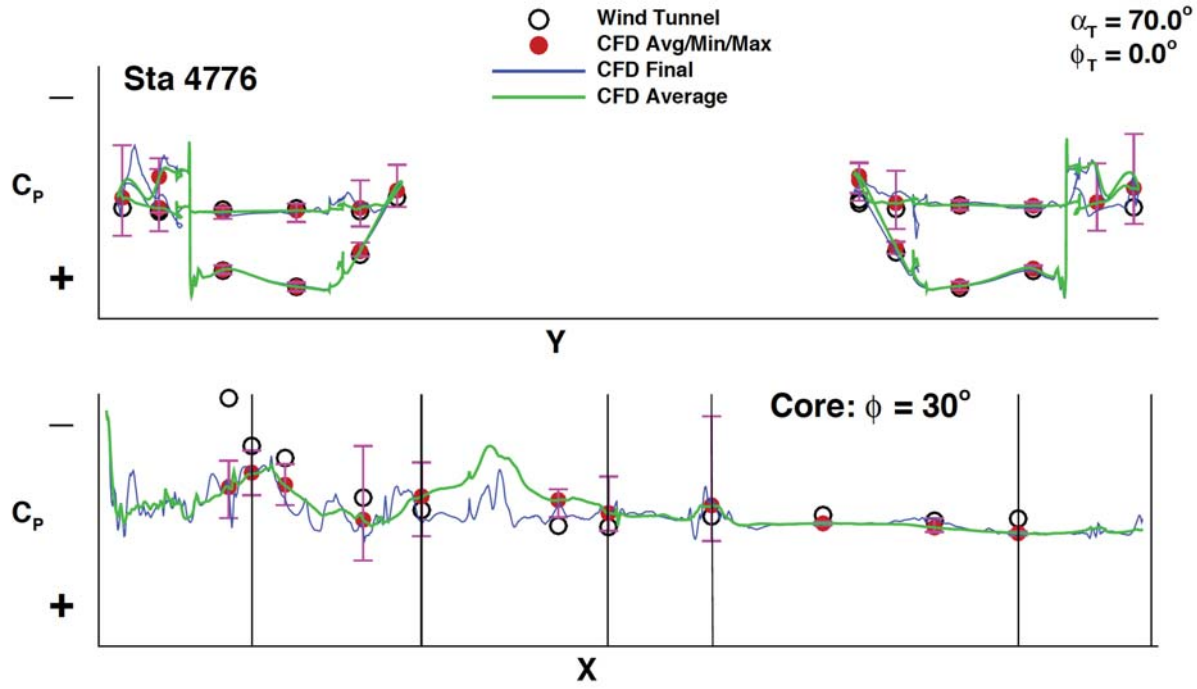

Figure 15. Pressure coefficient from wind tunnel data and CFD DES k-ε results for $\alpha_T = 70^o$, $\phi_T = 0^o$ at station 4776 and along the leeward side of the core stage at $\phi = 30^o$.

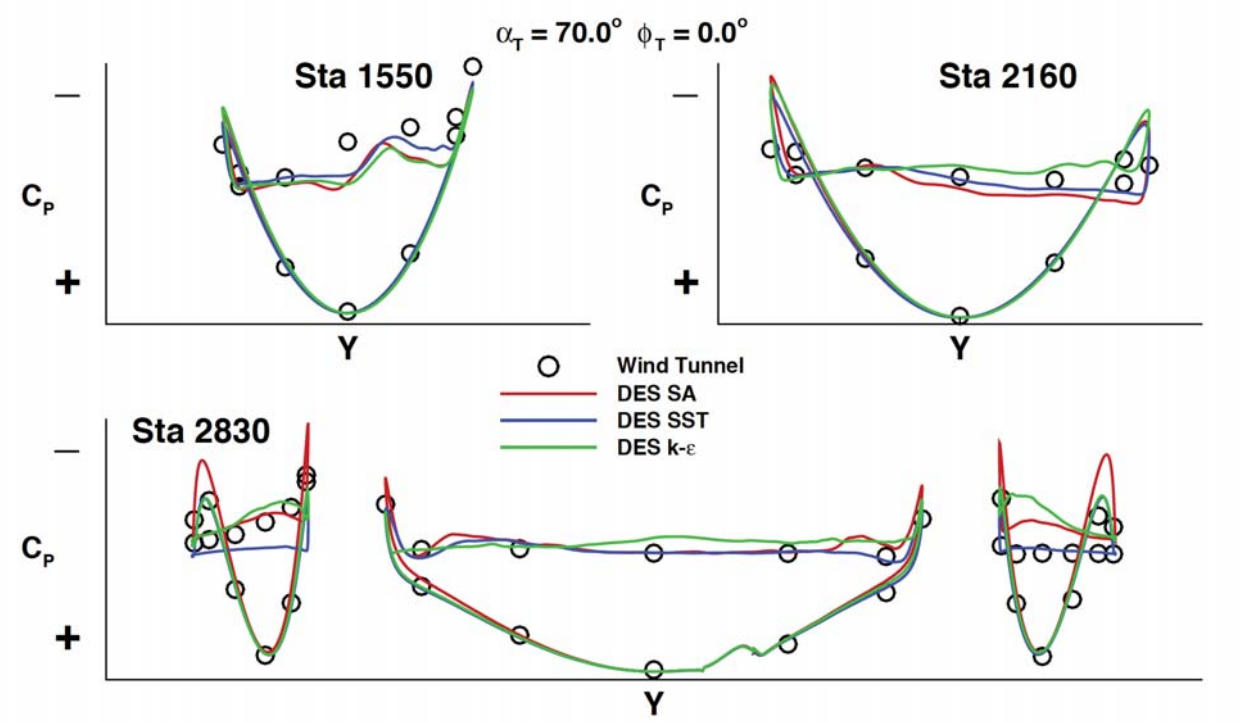

Figure 16. Pressure coefficient from wind tunnel data and CFD DES results with the SA, SST and k-ε turbulence models for $\alpha_T = 70^o$, $\phi_T = 0^o$ at stations 1550, 2160, and 2830

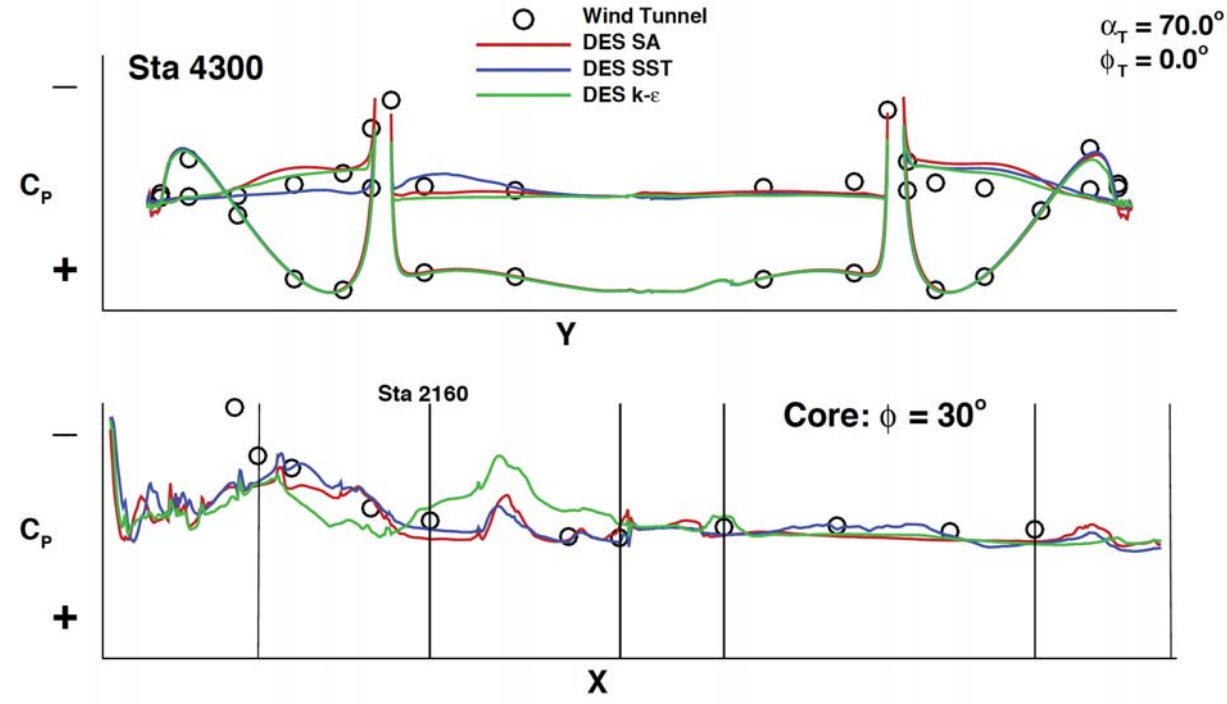

Figure 17. Pressure coefficient from wind tunnel data and CFD results with the SA, SST and k-ε turbulence models for $\alpha_T = 70^o$, $\phi_T = 0^o$ at stations 4300 and along the leeward side of the core stage at $\phi = 30^o$.

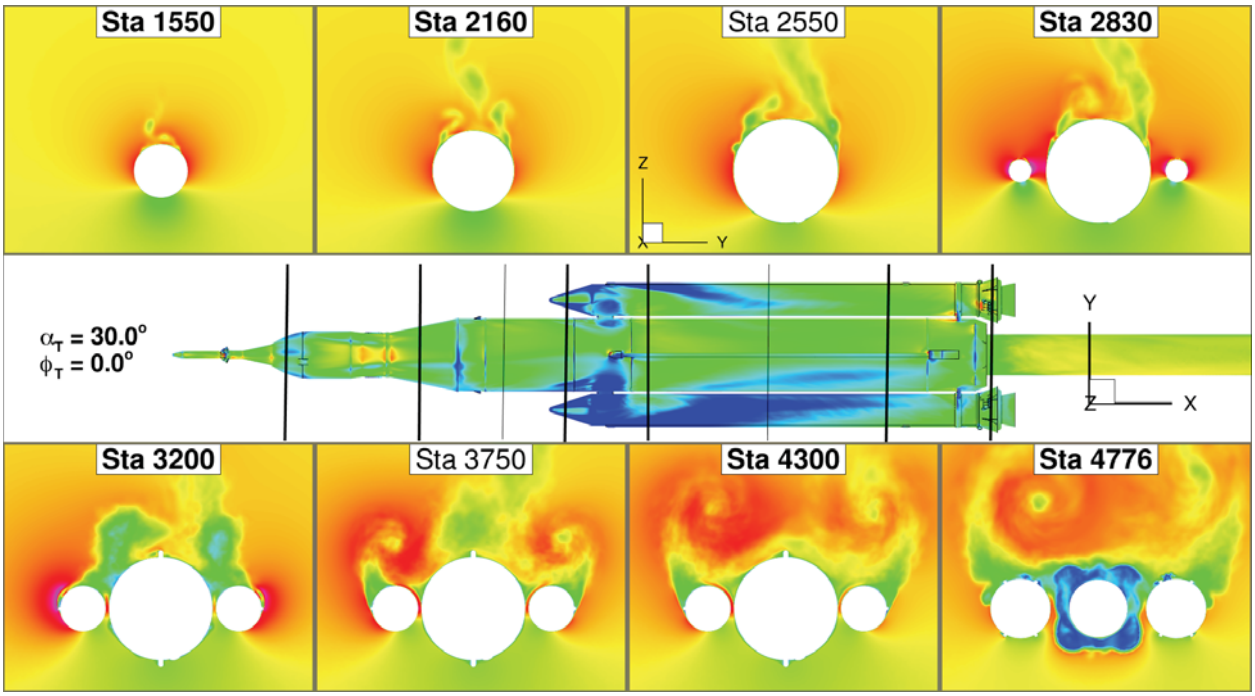

Figure 18. Time-averaged leeward surface pressure coefficient (planform) and crossflow Mach contours from the DES k-ε simulation at $\alpha_T = 30^o$, $\phi_T = 0^o$.

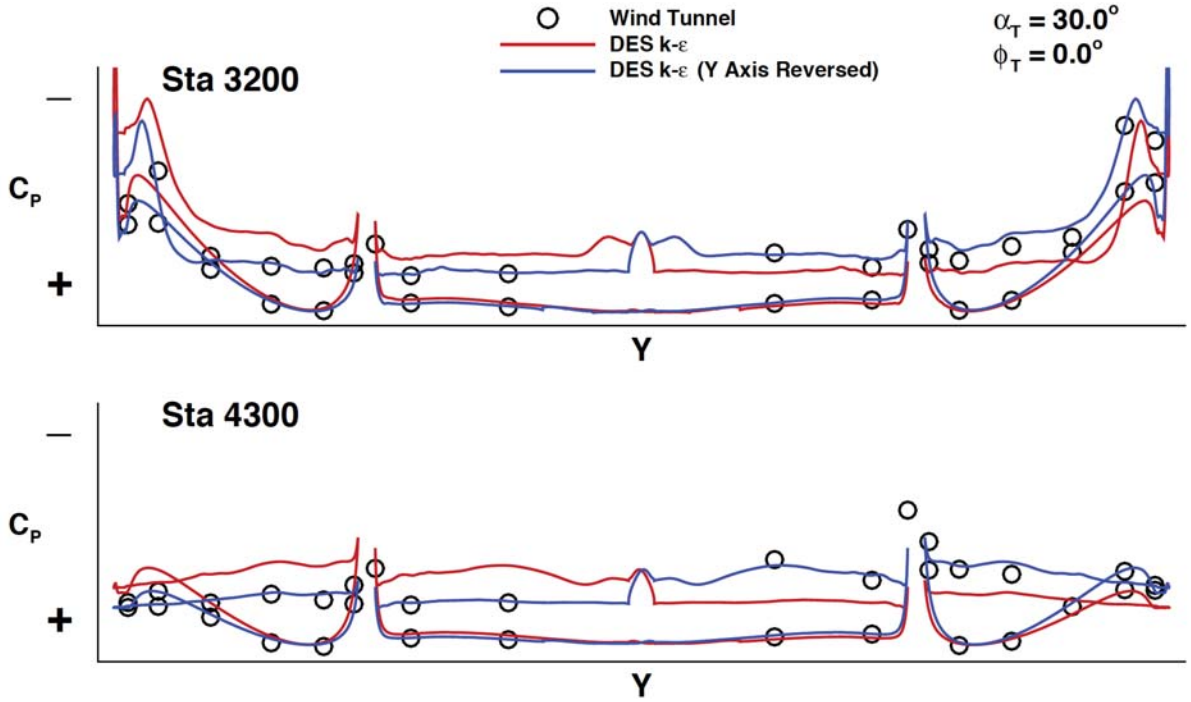

Figure 19. Pressure coefficient from wind tunnel data and DES k-ε results at $\alpha_T = 30^o$, $\phi_T = 0^o$ for the actual computed data (red) and the reversed data in the -Y coordinate (blue).

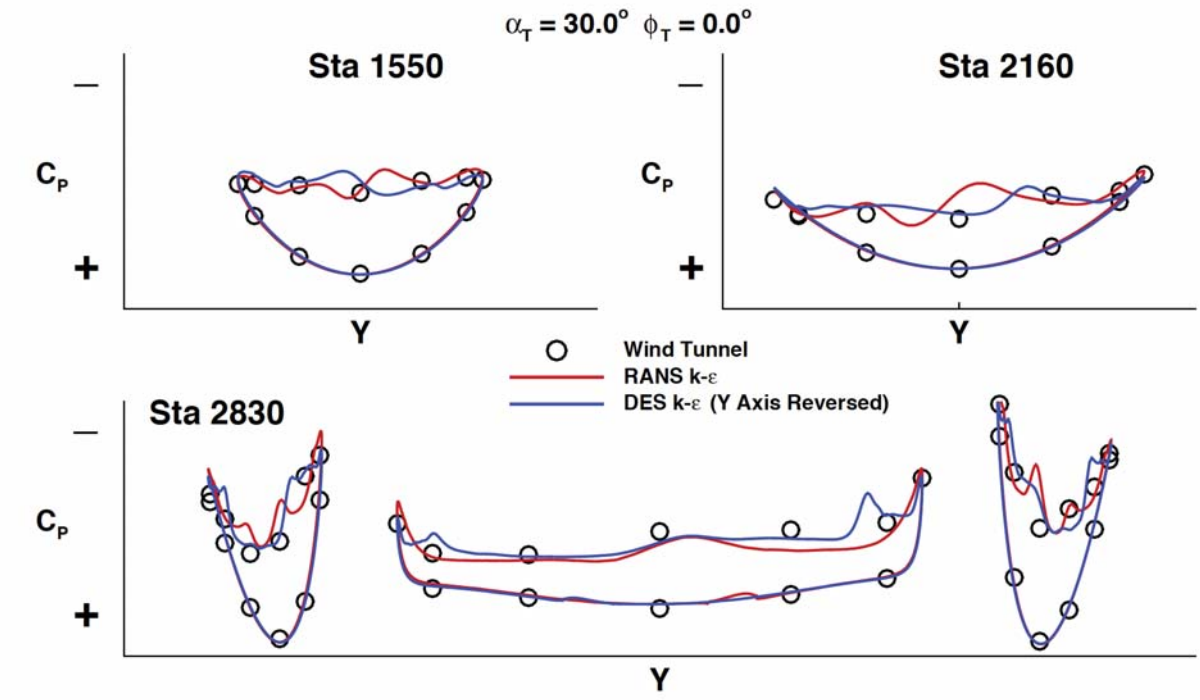

Figure 20. Pressure coefficient from wind tunnel data and CFD results at $\alpha_T = 30^o$, $\phi_T = 0^o$ for RANS k-ε (red) plotting the actual Y coordinate and DES k-ε (blue) plotting the –Y coordinate.

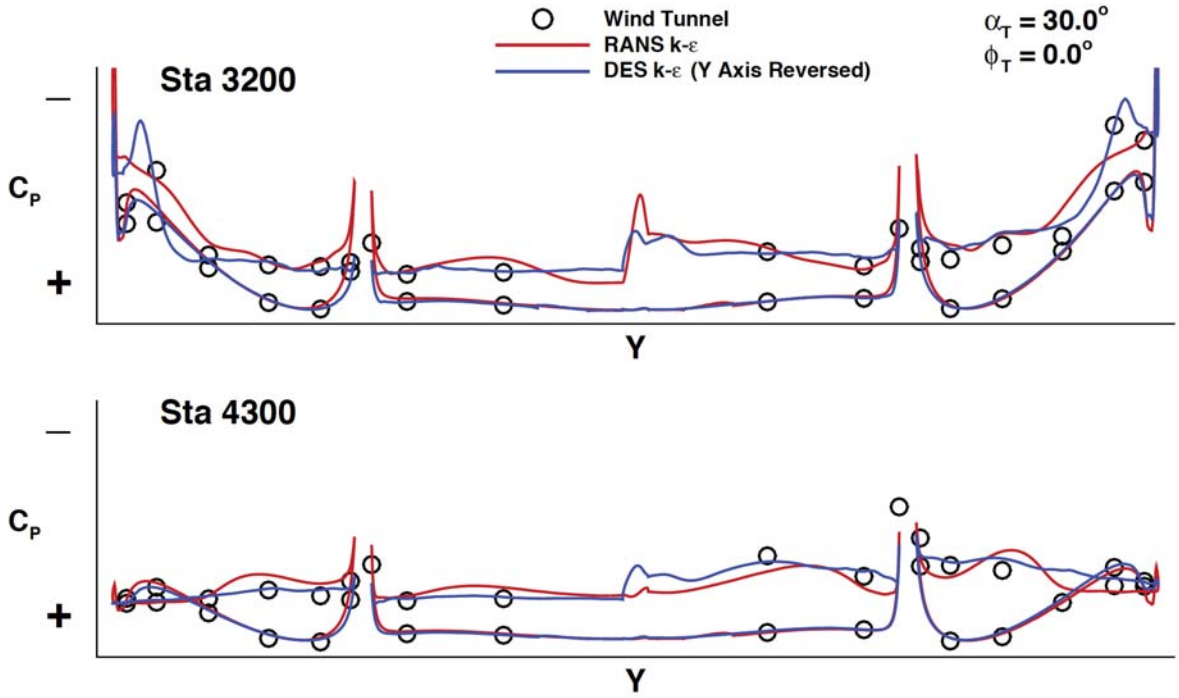

Figure 21. Pressure coefficient from wind tunnel data and CFD results at $\alpha_T = 30^o$, $\phi_T = 0^o$ for RANS k-ε (red) plotting the actual Y coordinate and DES k-ε (blue) plotting the –Y coordinate.

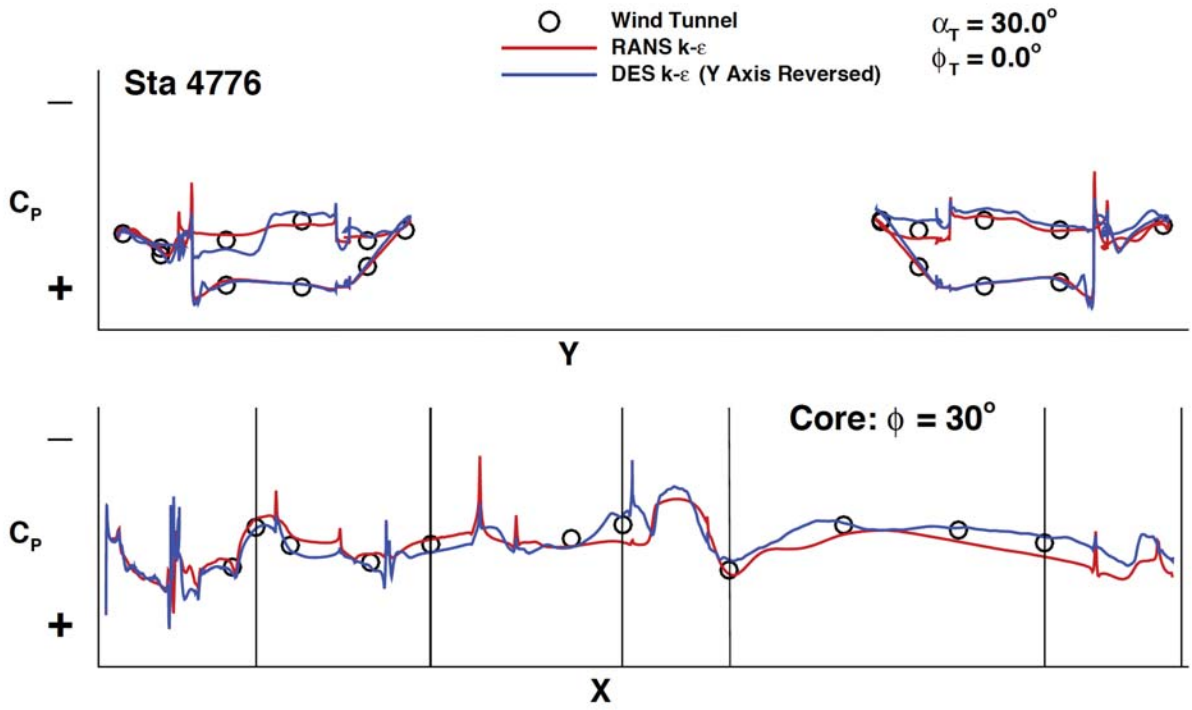

Figure 22. Pressure coefficient from wind tunnel data and CFD results at $\alpha_T = 30^o$, $\phi_T = 0^o$ for RANS k-ε (red) plotting the actual Y coordinate and DES k-ε (blue) plotting the –Y coordinate.